Icarus 222 (2013) 342–356

Contents lists available at SciVerse ScienceDirect

Icarus

journal homepage: www.elsevier.com/locate/icarus

Climatology and first-order composition estimates of mesospheric clouds from Mars Climate Sounder limb spectra

E. Sefton-Nash [a,*], N.A. Teanby [a], L. Montabone [b,c], P.G.J. Irwin [b], J. Hurley [b], S.B. Calcutt [b]

[a] School of Earth Sciences, University of Bristol, Queen's Road, Bristol BS8 1RJ, UK
[b] Atmospheric, Oceanic and Planetary Physics, University of Oxford, Oxford, UK
[c] Laboratoire de Météorologie Dynamique, Université Pierre et Marie Curie, Paris, France

ARTICLE INFO

Article history:
Received 30 April 2012
Revised 7 November 2012
Accepted 7 November 2012
Available online 27 November 2012

Keyword:
Mars
Mars, climate
Mars, atmosphere
Infrared observations
Atmospheres, dynamics

ABSTRACT

Mesospheric clouds have been previously observed on Mars in a variety of datasets. However, because the clouds are optically thin and most missions have performed surface-focussed nadir sounding, geographic and seasonal coverage is sparse. We present new detections of mesospheric clouds using a limb spectra dataset with global coverage acquired by NASA's Mars Climate Sounder (MCS) aboard Mars Reconnaissance Orbiter. Mesospheric aerosol layers, which can be CO_2 ice, water ice or dust clouds, cause high radiances in limb spectra, either by thermal emission or scattering of sunlight. We employ an object recognition and classification algorithm to identify and map aerosol layers in limb spectra acquired between December 2006 and April 2011, covering more than two Mars years. We use data from MCS band A4, to show thermal signatures of day and nightside features, and A6, which is sensitive to short wave IR and visible daytime features only. This large dataset provides several thousand detections of mesospheric clouds, more than an order of magnitude more than in previous studies.

Our results show that aerosol layers tend to occur in two distinct regimes. They form in equatorial regions (30°S–30°N) during the aphelion season/northern hemisphere summer ($L_s < 150°$), which is in agreement with previous published observations of mesospheric clouds. During perihelion/dust storm season ($L_s > 150°$) a greater number of features are observed and are distributed in two mid-latitude bands, with a southern hemisphere bias. We observe temporal and longitudinal clustering of cloud occurrence, which we suggest is consistent with a formation mechanism dictated by interaction of broad temperature regimes imposed by global circulation and the propagation to the mesosphere of small-scale dynamics such as gravity waves and thermal tides.

Using calculated frost point temperatures and a parameterization based on synthetic spectra we find that aphelion clouds are present in generally cooler conditions and are spectrally more consistent with H_2O or CO_2 ice. A significant fraction has nearby temperature retrievals that are within a few degrees of the CO_2 frost point, indicating a CO_2 composition for those clouds. Perihelion season clouds are spectrally most similar to H_2O ice and dust aerosols, consistent with temperature retrievals near to the clouds that are 30–80 K above the CO_2 frost point.

© 2012 Elsevier Inc. All rights reserved.

1. Introduction

Martian mesospheric clouds have been detected using a variety of infrared, ultraviolet and visible wavelength datasets at various points in the martian day and year, but limited spatial and seasonal coverage of observations has resulted in gaps in our understanding of cloud occurrence and composition over the martian globe and throughout the martian year. Aerosol layers are composed of either dust, water ice or CO_2 ice, but a wide range of physical parameters contribute to their spectral signature, which makes unambiguous identification of the their composition challenging. However, information pertaining to cloud composition is often discussed via retrieval and analysis of their associated pressure–temperature conditions and comparison of broad spectral characteristics to those of modelled spectra.

Detached layers composed of mesospheric dust aerosols were first observed in Mariner 9 limb measurements (Anderson and Leovy, 1978). Dust clouds up to 50 km have been identified in Viking limb images (Jaquin et al., 1986) and brightness maxima at up to 70 km altitude have been reported during southern summer ($L_s \gtrsim 180°$) (Jaquin, 1988). Maxima between 50 and 70 km were also observed in visible and infrared limb observations by NASA's Thermal Emission Spectrometer (TES) during the 2001 dust storm (Cantor, 2007; Clancy et al., 2003), while Smith (2003) calculated

* Corresponding author. Present address: Department of Earth and Space Sciences, University of California, Los Angeles, CA 90095-1567, USA.
E-mail address: esn@ucla.edu (E. Sefton-Nash).

0019-1035/$ - see front matter © 2012 Elsevier Inc. All rights reserved.
http://dx.doi.org/10.1016/j.icarus.2012.11.012

high dust optical depths above five scale heights (~50 km) for southern summer.

Detections from orbit of mesospheric clouds at visible wavelengths were made using Mars Orbital Camera (MOC) limb images acquired during Mars Years 24–26. Detections were corroborated by spatially and temporally coincident nadir spectra acquired by TES. Results showed a typical altitude range of 60–80 km but cloud composition could not be determined (Clancy et al., 2004).

However, the lack of detectable infrared radiances at these altitudes led Clancy et al. (2007) to constrain particle sizes to $\leqslant 1$ μm for water and $\leqslant 1.5$ μm for CO_2 ice compositions. CO_2 ice clouds have been spectrally identified in data from ESA's OMEGA imaging spectrometer (Montmessin et al., 2007; Scholten et al., 2010; Määttänen et al., 2010; Vincendon et al., 2011) and NASA's CRISM imaging spectrometer (Vincendon et al., 2011).

However, some high-altitude clouds that were previously classified as CO_2 ice in SPICAM observations (Montmessin et al., 2006) might be instead of water ice composition, as suggested by one OMEGA limb observation of an H_2O ice cloud observed at similar longitudes and season (Vincendon et al., 2011). This is consistent with the fact that no instrument sensitive to CO_2 ice appears to have observed the peak in occurrence of mesospheric equatorial clouds at $145° \leqslant L_s \leqslant 160°$ identified by Clancy et al. (2007). Many authors have suggested a water ice composition for some mesospheric clouds below about 80 km (Clancy et al., 2004, 2007; Fedorova et al., 2009; McConnochie et al., 2010; Vincendon et al., 2011).

So called 'blue wave' clouds observed above 70 km altitude were imaged by the Pathfinder camera (Smith et al., 1997) and were suggested to be composed of CO_2 ice, rather than water ice aerosols (Clancy and Sandor, 1998), since temperatures derived from a density profile inferred from the spacecraft's deceleration during descent were below the CO_2 condensation temperature between approximately 79–85 km (Schofield et al., 1997). Aerosol layers and proximal super-cold (below CO_2 condensation temperature) pockets detected between 80 and 100 km using stellar occultation techniques and data from the SPICAM ultraviolet spectrometer aboard Mars Express, led Montmessin et al. (2006) to hypothesise that they could be CO_2 ice clouds.

Early retrievals of martian dayside mesospheric temperatures were performed using data returned by the Mariner 6 and 7 (Herr and Pimentel, 1970) and Viking missions (Seiff and Kirk, 1977) as well as from observations using CO_2 laser emission (Deming et al., 1983; Johnson et al., 1976) and stellar occultation techniques (Montmessin et al., 2006). However, the wide range of retrieved mesospheric temperatures has encouraged debate as to whether atmospheric conditions frequently become cool enough to form CO_2 ice clouds or whether water ice or dust is a more likely candidate. Using modelled spectra to distinguish between water ice and CO_2 ice is often challenging due to the large number of unknowns regarding aerosols such as particle shape, heterogeneous cloud structure, line of sight effects, scattering by low altitude clouds with heterogeneous structure, and scattering of radiance from the unconstrained lower atmosphere.

Potential causes of mesospheric clouds have been reported as convection (Montmessin et al., 2007) thermal tides (Clancy and Sandor, 1998; Clancy et al., 2007; Forbes and Miyahara, 2006; González-Galindo et al., 2011; Lee et al., 2009; Määttänen et al., 2010) and 'cold pockets' (Clancy and Sandor, 1998) formed by conditions favouring the propagation of gravity waves into the mesosphere (Spiga et al., 2012).

Conditions associated with cloud formation have been compared to output from the Laboratoire de Météorologie Dynamique (du CNRS) global circulation model (LMD-GCM) (Forget et al., 1999, 2008) by González-Galindo et al. (2011) and to output from the LMD Mesoscale GCM (Spiga and Forget, 2009) by Spiga et al. (2012). In general mesospheric temperature retrievals are occasionally below the condensation point of CO_2, but models do not usually predict sub-CO_2 frost point temperatures at mesospheric altitudes (work by Colaprete et al. (2008) is an exception to this trend). This disagreement may be explained by interaction of cold atmospheric regions created by global circulation and the propagation to the mesosphere of small-scale dynamics such as gravity waves and thermal tides, which adiabatically reduce temperatures in rarefactions (González-Galindo et al., 2011; Määttänen et al., 2010; Spiga et al., 2012).

A full understanding of temporal and geographic distribution of clouds remains unconstrained due to limitations in data coverage, since clouds are observed coincidentally in nadir or rare limb observations. However, based on previously available detections, two distinct mesospheric cloud populations are observed in latitude-L_s space: equatorial clouds observed during northern summer, and mid-latitude clouds that tend to occur around the winter solstices in both hemispheres. There are a small number of observations of both types of clouds during local autumn (Clancy et al., 2004, 2007; Formisano et al., 2006; Inada et al., 2007; Määttänen et al., 2010; McConnochie et al., 2005, 2010; Montmessin et al., 2006, 2007; Scholten et al., 2010).

We present new detections of mesospheric clouds using data from NASA's Mars Climate Sounder (MCS) aboard Mars Reconnaissance Orbiter (MRO). MRO's Sun-synchronous polar orbit does not allow MCS to resolve daily cloud formation trends, but does provide near continuous atmospheric coverage. In addition, MCS' limb-sounding observation strategy enables greater sensitivity to optically thin clouds.

In this paper, we describe an algorithm to detect mesospheric aerosol layers based on the fact that they form high radiance arch-shaped loops in gridded limb spectra (due to observation geometry). The algorithm's detection and classification criteria are used to discern loops from background noise and non-loop features. We discuss the spatiotemporal distribution of positive detections made using more than two Mars years of gridded limb-spectra in two wavebands (MCS channels A4 and A6). Finally, we consider possible aerosol composition by analysis of the nearest available temperature–pressure retrievals for each loop and comparison of loop spectra with a wide range of synthetic spectra calculated for dust, water ice and CO_2 ice aerosol layers.

2. Observations

Mars Climate Sounder is a filter radiometer that measures thermal radiance in 9 spectral bands, with 21 pixels in each band (McCleese et al., 2007). Spectra are acquired in nadir sounding, polar buckshot scanning and along track limb-staring observation modes. Limb sounding, with pixel arrays oriented perpendicular to Mars' limb, is the primary observation mode and has returned a large dataset of atmospheric observations between 0 and 80 km altitude, acquired nearly continuously since Mars Reconnaissance Orbiter entered orbit in late 2006.

MCS has two symmetric telescopes, with separate focal planes A&B. Spectral channels cover the visible to far infrared (0.3–45 μm). Focal plane A has 6 bands. A1–5 cover the mid-IR and have band passes between 0.55 and 5 μm wide, while band A6 spans a wide interval from the visible to mid-infrared (0.3–3 μm). Focal plane B has 3 bands in the far infrared (with band centres at 31.7, 41.7 and 42.1 μm, respectively), located primarily to retrieve temperatures and water vapour below 40 km. However, due to the increased width of band B3 in the flight instrument it has so far not been possible to retrieve H_2O profiles.

In this study we use data returned from band A4 (11.5–12.2 μm), designed for measuring dust and condensate extinction

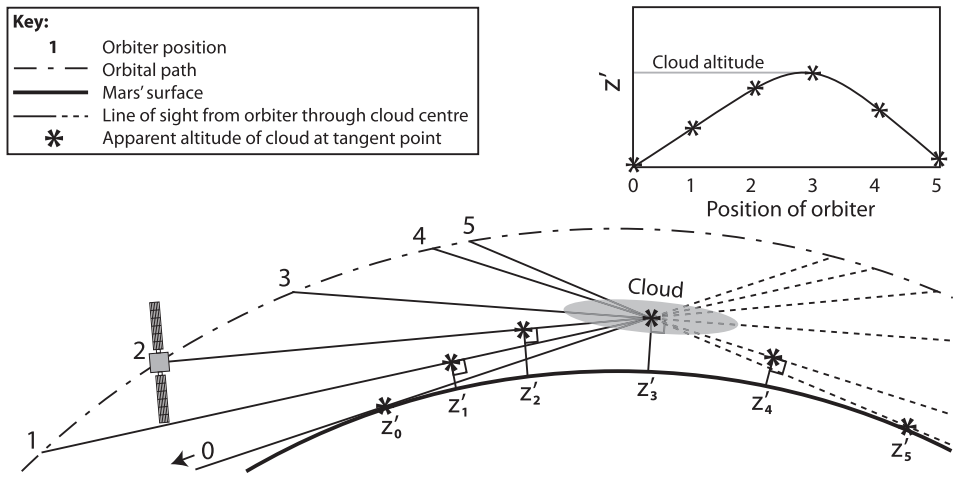

Fig. 1. The altitude of the tangent point of the line of sight (z') to the cloud gives projected apparent altitude of the cloud at each orbital position. The orbital path of the spacecraft causes the apparent altitude to increase then decrease as the cloud is viewed from below (0,1,2), edge on (3) and from above (4,5). This causes a discrete cloud to appear as a continuous loop in the radiance profile, which is acquired along-track. The apex of a loop gives the true altitude of a discrete cloud.

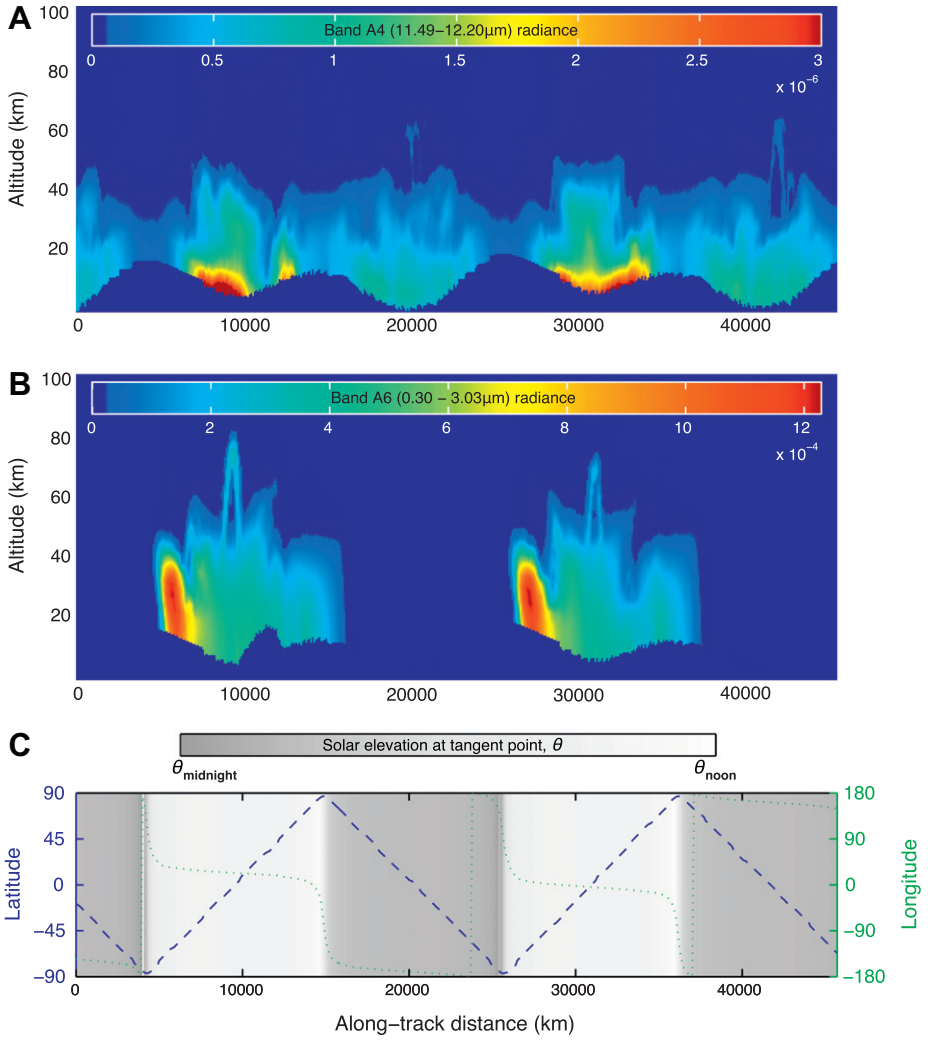

Fig. 2. Example of gridded limb radiance profiles from a 4 h sequence of MCS observations (Product ID: 080123040000). Each column of pixels in the top two panels is derived from an average of five adjacent individual limb measurements (referred to as a block). Each product contains several hundred blocks, typically acquired over approximately two orbits, that are gridded onto a linear distance scale representing the along-track nadir path. (A) Band A4, with a central wavelength of 11.8 μm, shows thermal signatures of loop features on the day and night-side. (B) Band A6, with a central wavelength of 1.65 μm and a wide band-pass of 0.303–3.03 μm, is more sensitive to loop features, but only in dayside spectra. (C) Latitude and longitude of tangent point against along-track distance for the two orbits. Gray shading indicates the solar elevation relative to the surface at the tangent point, i.e. grey areas represent the night side.

in the altitude range 0–80 km (McCleese et al., 2007), and band A6, which covers a broad range in the visible to short-wave infrared (0.3–3 μm). Band A6 relies on reflected solar band radiance so features we detect in band A6 data are almost entirely limited to the dayside. We also analyse radiances from bands B1 and B2 to illustrate broad spectral trends over season.

MRO's orbit lasts 112 min 12 s and has an inclination of 92.6°, which ensures full latitudinal coverage and results in a dayside equator crossing local time of 15:00. Orbital altitude varies between a 255 km periapsis (over the south pole) and a 320 km apoapsis (over the north pole). MCS limb and nadir observations are normally acquired in the same observation–calibration sequence, which lasts ~34 s. In this time 2 nadir observations are followed by 8 limb observations, although an actuator anomaly in January 2007 resulted in a modified observation strategy, comprising limb-stare interspersed with off-nadir surface views. Finally, to correct for the effects of thermal drifts, two calibration observations are made, one of deep space and one of a black body calibration target mounted on the instrument yoke. In one sequence, the average horizontal along-track spacing of limb observations (comprising a complete atmospheric profile, or 21 spectra) is 110 km, but regularly spaced gaps in data coverage occur between sequences due to acquisition of calibration and nadir spectra. Twenty-one pixels in each spectra represent radiance at 21 altitudes, typically covering −10–100 km altitude. The vertical spacing of pixels is 5 km, which is approximately equal to half the atmospheric scale-height (McCleese et al., 2007).

3. Cloud detection

A characteristic of the limb observation geometry is such that measured radiance contains contributions from the instrument's entire line of sight, which is tangential to the surface and passes through a range of altitudes in the atmosphere. As a result, in successive spectra obtained as the spacecraft orbits, discrete radiance features such as aerosol layers/clouds show different apparent altitudes in the instruments' focal plane. Their altitude projected onto the instruments will at first lie near the surface, as the feature appears on the horizon (Fig. 1 – position 0). Successive spectra will show its apparent altitude rise (positions 1 and 2) to reach an apex when the line of sight is tangential to the surface (position 3), which is equal to the feature's true altitude. Finally the feature's projected altitude will fall again as the spacecraft passes over it (positions 4 and 5). The resulting 'loop'-shaped structure is distinct and can be used as a signature for detection of discrete clouds, most notably at mesospheric altitudes where there are few other major radiance features.

4. Preprocessing

We started with calibrated and geometrically registered level 1B data from the standard pipeline (Henderson et al., 2007; McCleese et al., 2007). First, averaging was applied to spectra to increase the signal to noise ratio. Limb spectra were taken in groups of eight, however the first three spectra after a black body calibration could be affected by high temperature transients (Kleinbohl et al., 2009a). We therefore averaged the last five points in each sequence of eight and rejected the first three. Second, the altitude, latitude and longitude of the tangent point of each pixel was determined using ray-tracing (Teanby, 2009). Altitudes of geometrically registered spectra were relative to the surface as represented by four pixel per degree gridded data from the Mars Orbiter Laser Altimeter (MOLA) (Zuber et al., 1992) aboard NASA's Mars Global Surveyor. We converted altitudes relative to the surface into those relative to the aeroid, since a gravitational equipotential surface most closely follows atmospheric pressure contours. This was performed by subtracting the value of the MOLA surface and adding the value of the aeroid at the geographic coordinates of each spectra. Aeroid and surface grids were both stored at a resolution of 4 ppd and were co-registered. Bilinear interpolation using the nearest 4 grid points was performed in order to return values at specific geographic coordinates. Spectra were then resampled onto regular horizontal surface distance and altitude grids with 100 km horizontal and 0.5 km vertical spatial resolution (Fig. 2), which provide the starting point for feature detection.

The average along-track spacing for a block of 5 limb-spectra is 110 km (McCleese et al., 2007), but can vary between data products due to calibration measurements and off-nadir ground measurements. Artifacts, produced by gridding of sparsely spaced or variably-spaced spectra were found to cause false classifications of features, i.e. the algorithm reporting the presence of a loop where there was none. We found spacings of 400 km or less sufficient to resolve loops and avoid this problem. 2810 data files that

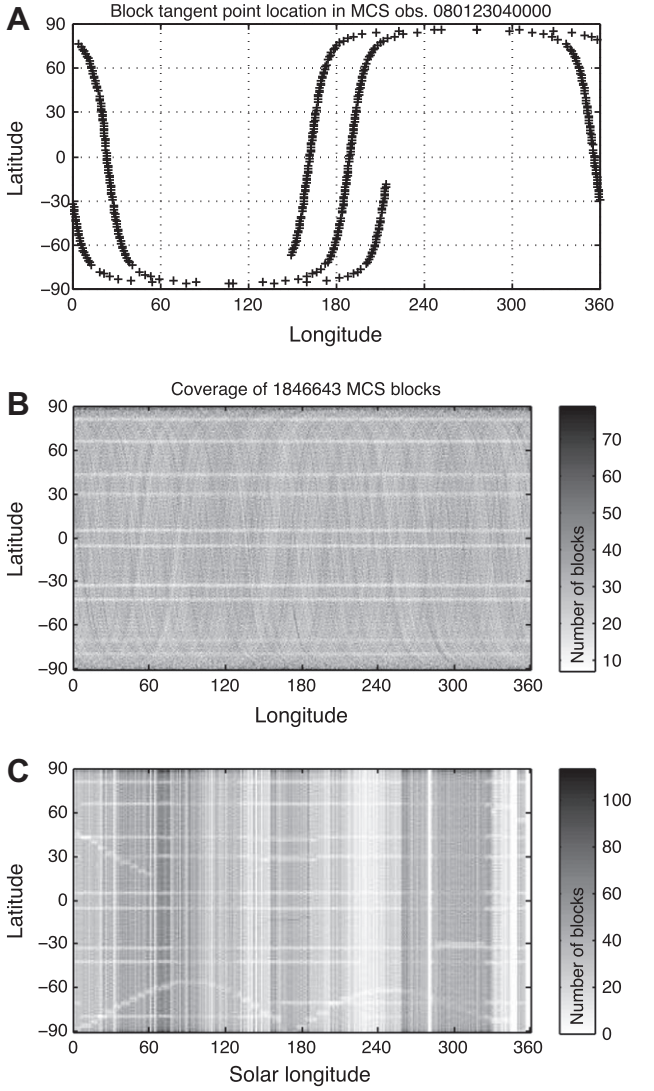

Fig. 3. (A) Example geographic coverage of one data product (Product ID 080123040000). Each cross represents the tangent point position of the boresight for a block. (B) Geographic coverage of all blocks used in this study. A total of 1846643 blocks are binned into 1° × 1° squares. (C) Temporal and latitude coverage. The total blocks used in this study are binned into 1° latitude × 1°L_s squares. B and C show that our dataset has excellent geographic and temporal cover.

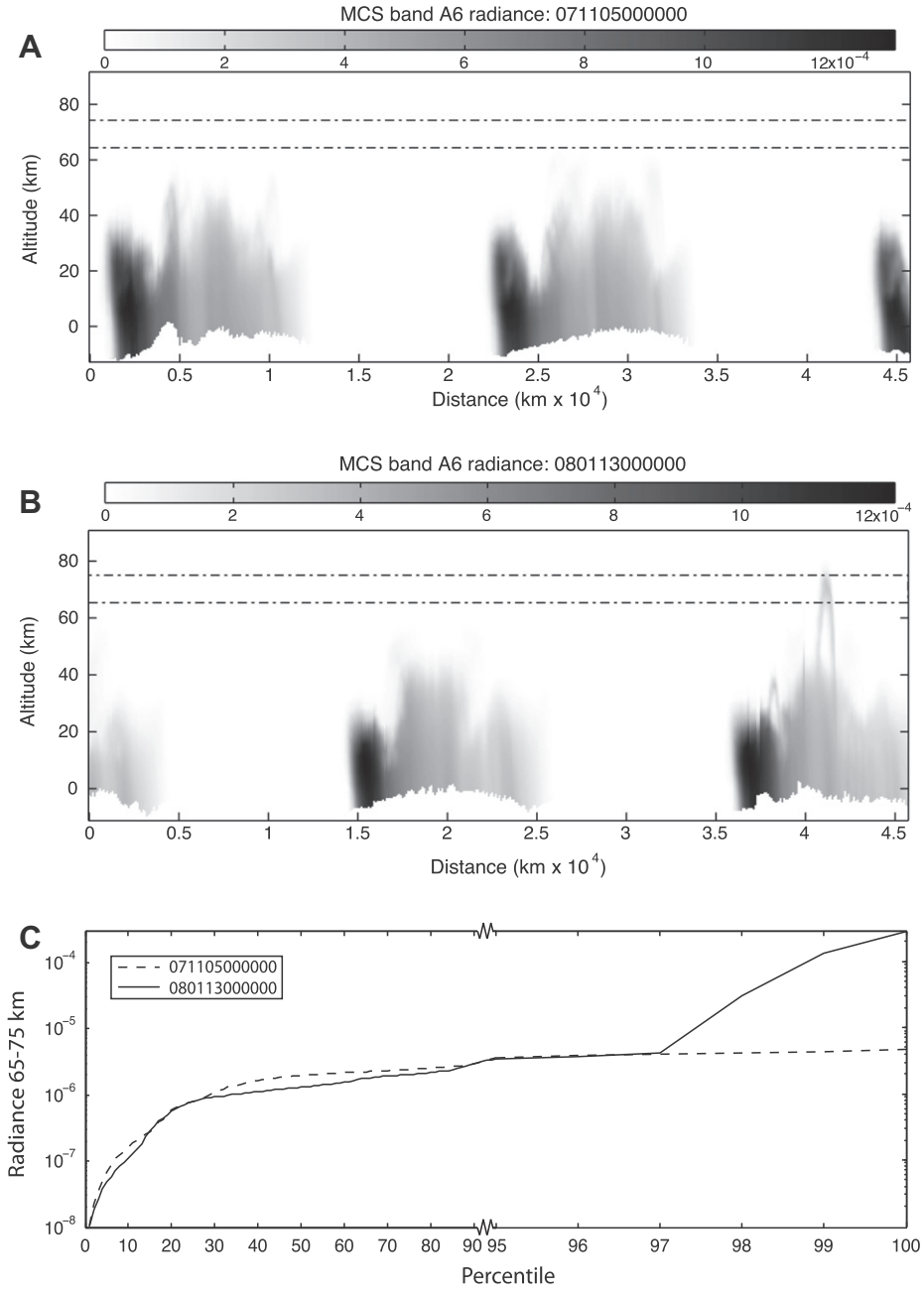

Fig. 4. Plots of A6 radiance in two MCS data products, one showing a loop feature and one not. (A) Product 071105000000 shows no loop features in the altitude range 65–75 km (enclosed with a dashed-dotted line). (B) Product 080113000000 shows a loop feature with an apex at approximately 70 km altitude. (C) Distribution of radiances in the 65–75 km altitude range in each plot. Radiances in product 080113000000 have high values relative to those in 071105000000 at high percentiles (97–100%). This illustrates that in the presence of loops a large fraction of the total radiance in this altitude interval lies in high radiance values.

contained spectra spaced more widely than this threshold were not used. We also rejected files that contained radiance values for bands A4 or A6 that were zero for sections or the length of the file, indicating calibration problems. Overall, 3898 data files acquired between December 2006 (MY 28) and April 2011 (MY 30) were used in this study, the spatial and temporal coverage of which is shown in Fig. 3.

4.1. Detection of loop features

Gridded data below 50 km altitude were discounted, since discrete layer features become swamped by lower atmosphere emission. Distance–altitude radiance grids (e.g. Fig. 2) were binarized into object matrices by thresholding using a radiance of 5×10^{-8} for band A4 and 1×10^{-4} nW cm^{-2} sr^{-1} cm^{-1} for band A6, which was chosen after testing of 25 random files that showed loop features (e.g. Fig. 4). Post binarization, the detection of loop features was performed using automated object analysis (Fig. 5). Binary images were converted to object matrices, where pixels representing a feature contained the integer identifier of that feature, while the background contained 0.

Features were classified as loops if they satisfied several numeric criteria, which were determined by running the algorithm on a representative subset of the data and manually classifying detected features as loops or not. We found that features that represented all or parts of loops had cross-sectional areas between 750

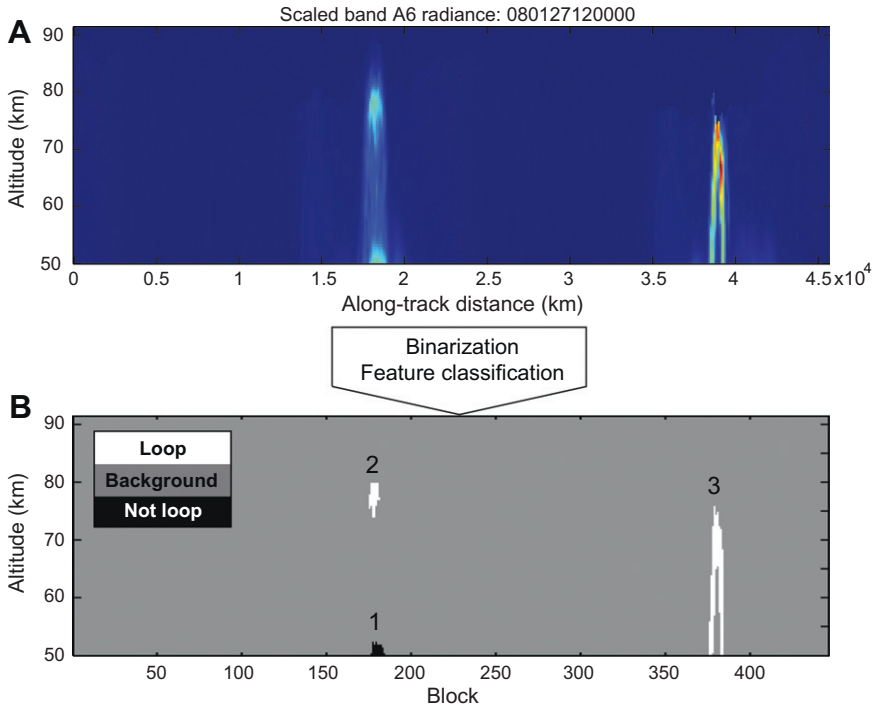

Fig. 5. Example illustrating the method used to determine (1) if there are features in a data file and (2) if they are loops, or visible parts of loops, likely to be formed by mesospheric clouds. (A) Band A6 radiance for MCS data product 080127120000 plotted for radiances above 50 km altitude. Two bright vertical linear features are apparent. (B) The results of binarization and classification of the image. They are produced by radiance thresholding. They are then classified based on cross-sectional area, aspect-ratio and orientation to determine if they are likely to be loop features. Ancillary information for positive matches (e.g. local time, latitude, longitude, altitude) is then stored. In this example two loops were found (labels 2 and 3).

and 22,500 km^2, major axes orientations within 10° of the vertical and had aspect ratios >2. These numerical criteria were therefore used as a basis for classification. Using these parameters, we found the algorithm achieved a 90% classification success rate compared to human classification on a test set of 100 randomly selected data products. The remaining 10% of features that were incorrectly classified were often upper portions of larger lower atmosphere features that had been isolated during thresholding and, coincidentally, had satisfied geometric criteria.

Complete loop structures were not required in object matrices to return a positive detection, since a loop's ascending and descending limbs can sometimes appear disconnected from its apex, making the total size of the feature appear small relative to a complete, connected loop (e.g. feature 2 in Fig. 5).

Non-loop features that commonly appeared in gridded data above 50 km were caused by temperature/dust anomalies and were most common during northern hemisphere winter ($150° < L_s < 360°$). Misclassification of these features as loops was rare, since they typically failed the aspect ratio and orientation tests.

While testing indicated that 90% of detected features appeared to be detached aerosol layers, we found that our algorithm did not detect all such layers, since some are quite subtle. Preliminary work by Kass et al. (2011) suggests that improvements to this technique may be possible by including all of MCS's available channels for detection. However, our approach was sufficient to detect major layers and thus illustrate broad geographic and seasonal trends.

5. Results

Fig. 6 shows the location of detected loop features in bands A4 and A6. We attribute these features to discrete high altitude (>50 km) aerosol layers or clouds. To remove observation bias we count the number of detections in bins of 5° latitude and 5° solar longitude, then divide by the number of observation blocks acquired in each bin (Fig. 7).

5.1. A6

Since band A6 has a bandpass in the visible to shortwave infrared (0.3–3 μm), features detected are visible only during daylight hours. Panel A of Fig. 6 therefore shows only dayside clouds. In Northern hemisphere summer, clouds are detected predominantly at equatorial latitudes, with higher frequency during L_s ranges 0–40° and 100–130°, on both sides of the northern hemisphere summer solstice (Fig. 6). This distribution is not seen during the dust storm/perihelion season, when we observe a paucity of clouds at equatorial latitudes. Instead, most positive detections tend to occur in two mid-latitude bands (~30–60°), with more detections in the Southern Hemisphere, particularly in the periods L_s = 150–190°, at the start of northern hemisphere fall, and 240–270°, prior to northern hemisphere winter solstice. The two regimes are separated by a sharp boundary at L_s = 150°, which loosely marks the beginning of dust storm season. We plot the geographic distribution in non-dust storm and dust storm conditions in Fig. 8 to highlight the disparity.

The distribution of clouds detected over latitude and season does not appear to differ greatly between each Mars year, when accounting for observational bias (Fig. 8, panel A). Analysis of cloud distribution in separate aphelion and perihelion seasons reveals little latitudinal variation within each seasons' regime. Aphelion season (northern hemisphere summer) cloud detections are generally concentrated between −50° and 50°N with very few clouds detected southwards of −60°N, at south polar latitudes (Fig. 8, panel B). Perihelion season (northern winter) cloud detections are concentrated along two mid-latitude bands, but with few detections

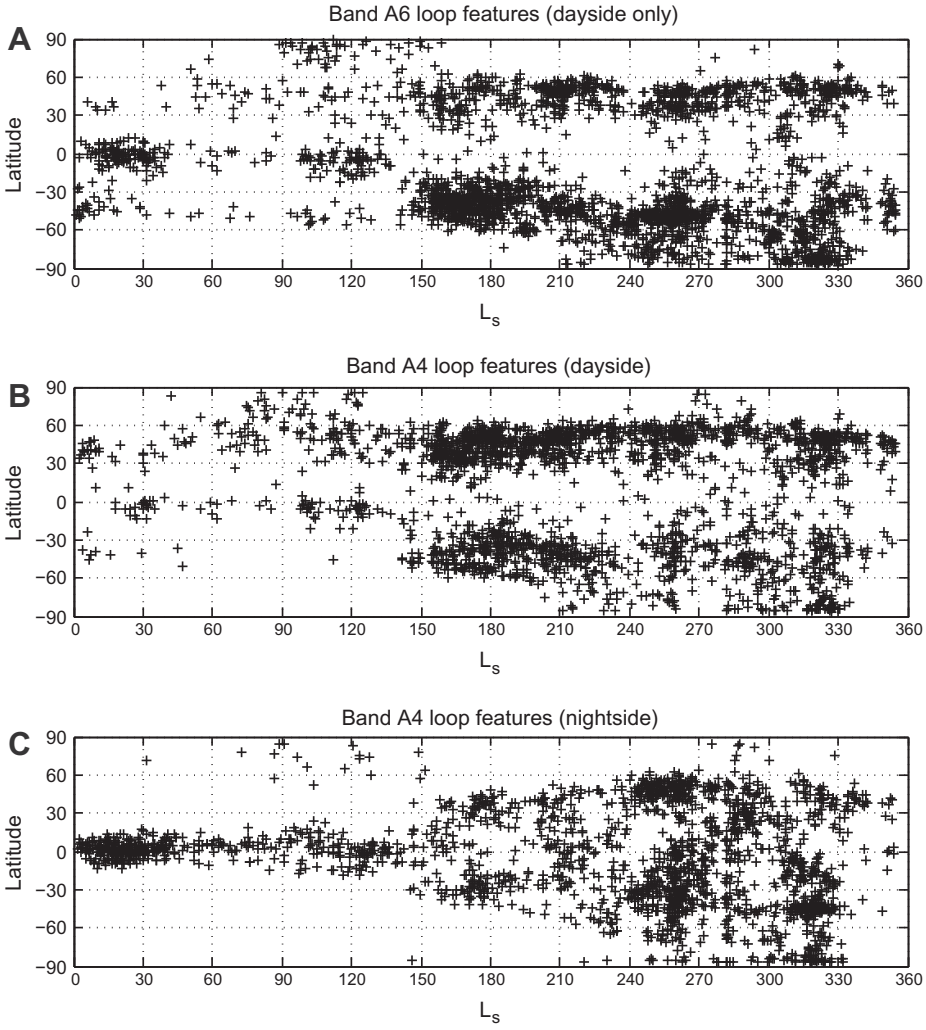

Fig. 6. Latitudes of detected loop features as a function of season in bands A4 and A6. (A) Band A6 loops. Due to the positioning of the band centre only dayside features are visible in A6. (B) Band A4 dayside loop features. (C) Band A4 nightside loop features.

around the equator, high detection frequency around the south polar region and almost no cloud detections northwards of 60° latitude (Fig. 8, panel C).

5.2. A4

We also ran the detection algorithm on data from mid infrared band A4 (11.49–12.20 μm). Increases in radiance in this band can be due to thermal emissions of condensates (McCleese et al., 2007) and therefore detections are not restricted to the dayside, but are possible at all local times. We plot the day and night-side distribution of clouds detected in band A4 (Fig. 6, panels B and C). For both day and night plots we see a generally similar spatio-temporal distribution of clouds to that detected in band A6. The main difference between day and night distributions as detected in band A4 is an increased number of clouds in the mid-latitude bands in the period L_s = 150–240°, during northern hemisphere fall.

Thermal signatures, from band A4, are more likely to produce false positive detections of loops than visible signatures from band A6, because high altitude temperature anomalies, particularly during the aphelion season (L_s < 150°), may appear in band A4, but not in band A6. Since we regard detections in band A6 as more reliable due to its much cleaner signal, we focus on the distribution of clouds over latitude, longitude, L_s and altitude in band A6 data in Figs. 8 and 9.

5.3. Altitude

We define cloud altitude as the uppermost pixel of a detected feature that satisfied the radiance threshold. Field of view leakage between successive spectra in a vertical profile can cause the edges of loop features in gridded spectra to appear more diffuse and as a result, the upper edges of clouds could be slightly higher than their reported altitude. However, the vertical extent of the object resulting from thresholding at the apex of a loop tends to be ~5 km and was not seen to exceed 10 km, consistent with previous estimates of cloud thickness (Montmessin et al., 2007; McConnochie et al., 2010). Since the vertical spacing of spectra in each block is 5 km, vertical structure finer than this cannot be resolved, hence reported altitudes are accurate to approximately ±2.5 km.

Altitudes of previously detected mesospheric clouds lie in the range 45–110 km (Clancy et al., 2004; Määttänen et al., 2010; McConnochie et al., 2010; Montmessin et al., 2006, 2007). On average we find the highest number of loop features in the range 55–65 km both in band A6 and in A4 (Fig. 9). However, a population of high altitude (80–90 km) features is detected in band A6, which is temporally concentrated almost exclusively between

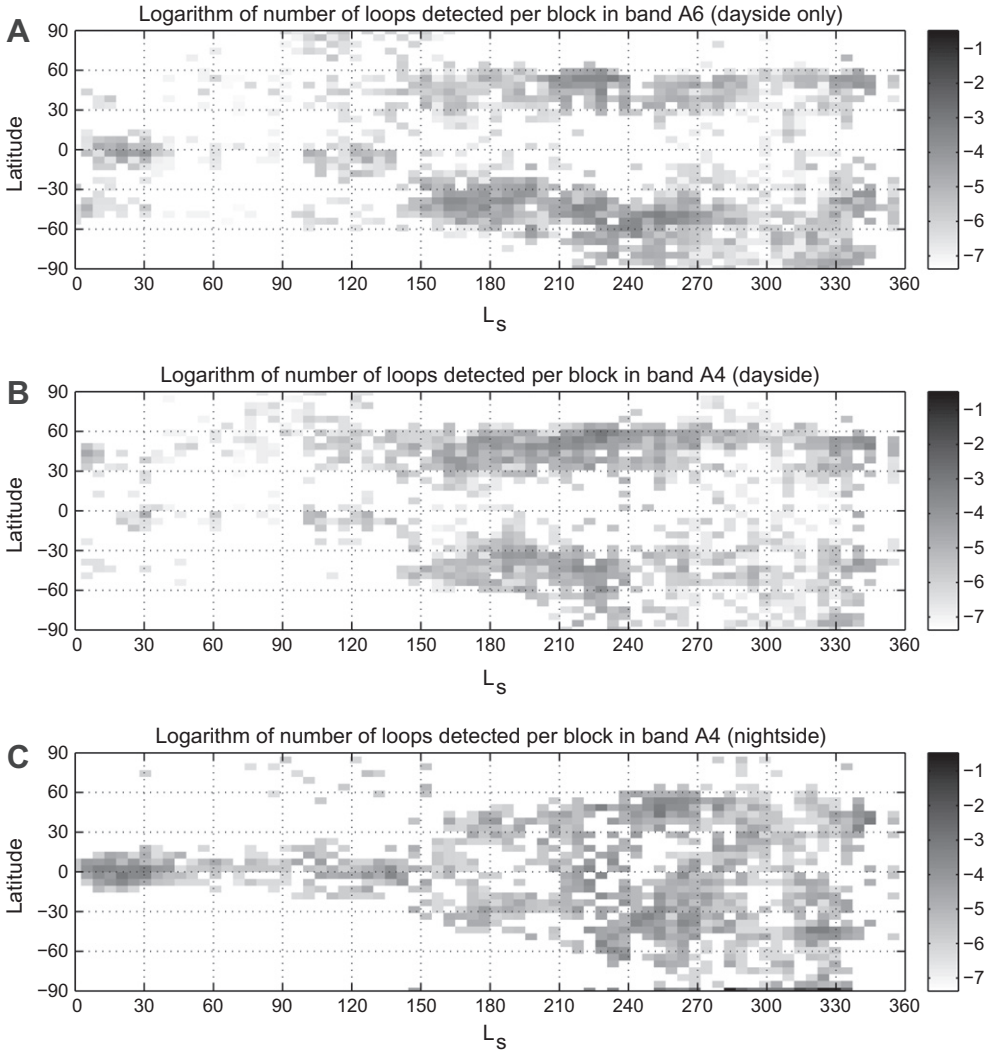

Fig. 7. Logarithm of the number of loops detected per block (to correct for observation bias) as a function of season in bands A4 and A6. The number of loops counted in 5° latitude and 5°L_s bins is divided by the number of blocks acquired in the same bin. Blocks are present in all bins and bins with no loops detected appear as white. (A) Band A6. Due to the positioning of the band centre only dayside features are visible in A6. (B) Band A4 dayside. (C) Band A4 nightside.

L_s = 250–270°, in northern mid-winter. We find this high-altitude population to be distributed mostly in a narrow latitude band centred around 45°S, with a few features located further towards the South Pole.

6. Discussion

6.1. Atmospheric temperature

Fig. 10 shows the MCS-derived temperature at 60 km and 80 km above the aeroid for Mars years 29 and 30 (as available in PDS level 2 DDRs derived by Kleinbohl et al. (2009b)) averaged for all observations within latitude-L_s bins of 5° i.e. over all longitudes and all local times. Some inter-annual variation is evident between the two Mars years, but seasonal trends are similar. We note similarities between the temperature distribution over L_s and latitude for detected clouds (Fig. 6) and the temperature trends observed by MCS. Specifically, cold equatorial and mid-latitude temperatures are observed for L_s < 150°, when we detect equatorial aerosol layers.

The coldest temperatures at 80 km occur prior to L_s = 150°, in northern summer, at approximately 60°S, but we do not detect a significant number of loops in that region. If clouds are composed of H_2O–ice, the lack of detections could be due to low water–vapour column abundance that is typical at that latitude and season, as observed by MGS-TES (Smith, 2004). Alternately, some other process that is crucial to cloud formation and not sensitive to temperature may not occur there.

Two mid-latitude bands are home to the coldest temperatures in Southern summer (perihelion season). The majority of features we detect form in these two latitude bands, with those detected at night (band A4) being more scattered in latitude than those detected during daylight hours (Fig. 6).

During L_s 240–280° a large number of features are detected over a wide range of altitudes, but unlike the rest of the martian year, particularly at altitudes >70 km (Fig. 9). During this period generally higher temperatures are observed by MCS, most noticeably at 60 km (Fig. 10). This correlation may be the result of warm southern hemisphere temperatures during perihelion season, which would be expected to cause increased upwelling. This interpretation is consistent with calculations of the convective available potential energy (CAPE) (Holton, 2004) from MCS P-T retrievals by Heavens et al. (2010), who associate high values of CAPE between L_s = 180–300° with convective instabilities. This could transport dust and water vapour to high-altitude, causing adiabatic cooling and subsequent condensation. In this case, increased dust loading

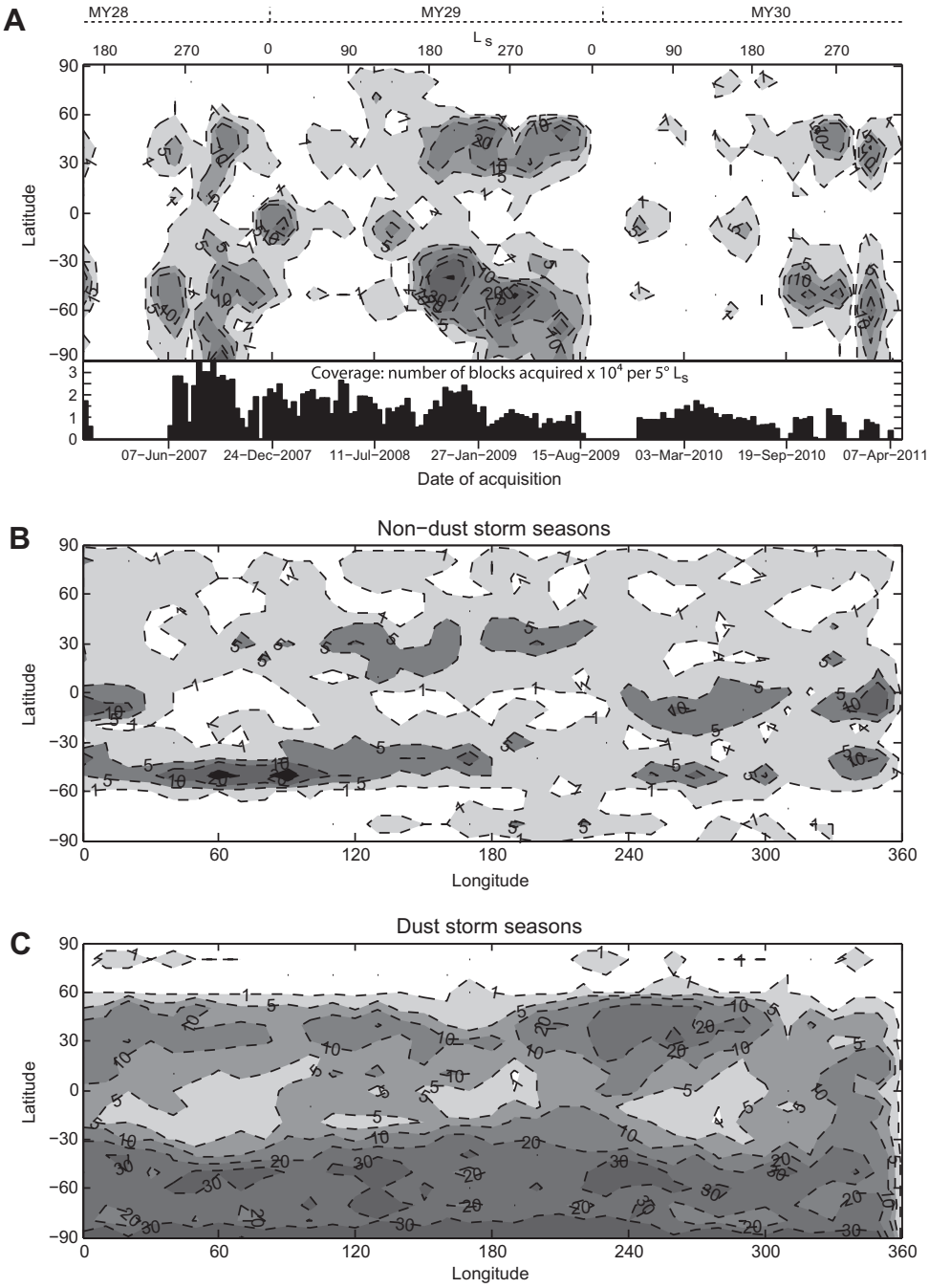

Fig. 8. Geographic and temporal distribution of loops as detected in band A6 data. (A) The occurrence of loops over latitude and time. Lower box shows observation bias: number of blocks acquired in each 5° of L_s over calendar time. (B) Occurrence of loops over latitude and longitude for northern summer ($0 \leqslant L_s < 150°$) is predominantly equatorial and distributed between −60° and 60°N. (C) Occurrence of loops over latitude and longitude for Northern winter ($150° \leqslant L_s < 360°$) is distributed along two mid-latitude bands, with slightly more detections in the southern hemisphere.

could provide an abundance of effective ice nucleation sites (Gondet et al., 2012; Määttänen et al., 2010; McConnochie et al., 2010).

6.2. Temperature deviation from CO_2 frost point

In order to provide discrimination between likely aerosol candidates we compare our observed mesospheric aerosol layer distribution to the nearest available atmospheric temperature and pressure retrievals. CO_2 ice is unlikely to be present if local atmospheric pressure and temperature does not result in CO_2 saturation. For each feature we therefore extract the atmospheric pressure and temperature from the PDS (level 2 DDRs) temperature profiles, which were retrieved using the method of Kleinbohl et al. (2009b). Deviation of P–T conditions from CO_2 saturation vapour pressure was calculated by using a polynomial fit to the experimental saturation vapour pressure data in Lide (1995) ($p(T) = \exp(A + B/T + CT)$, where $A = 25.24826$, $B = -3882.969$ K, and $C = -0.02722391$ K^{-1}, where $p(T)$ is the saturation vapour pressure in pascals). We retrieved the pressure for each feature and calculated the difference between the observed temperature and that required for CO_2 saturation.

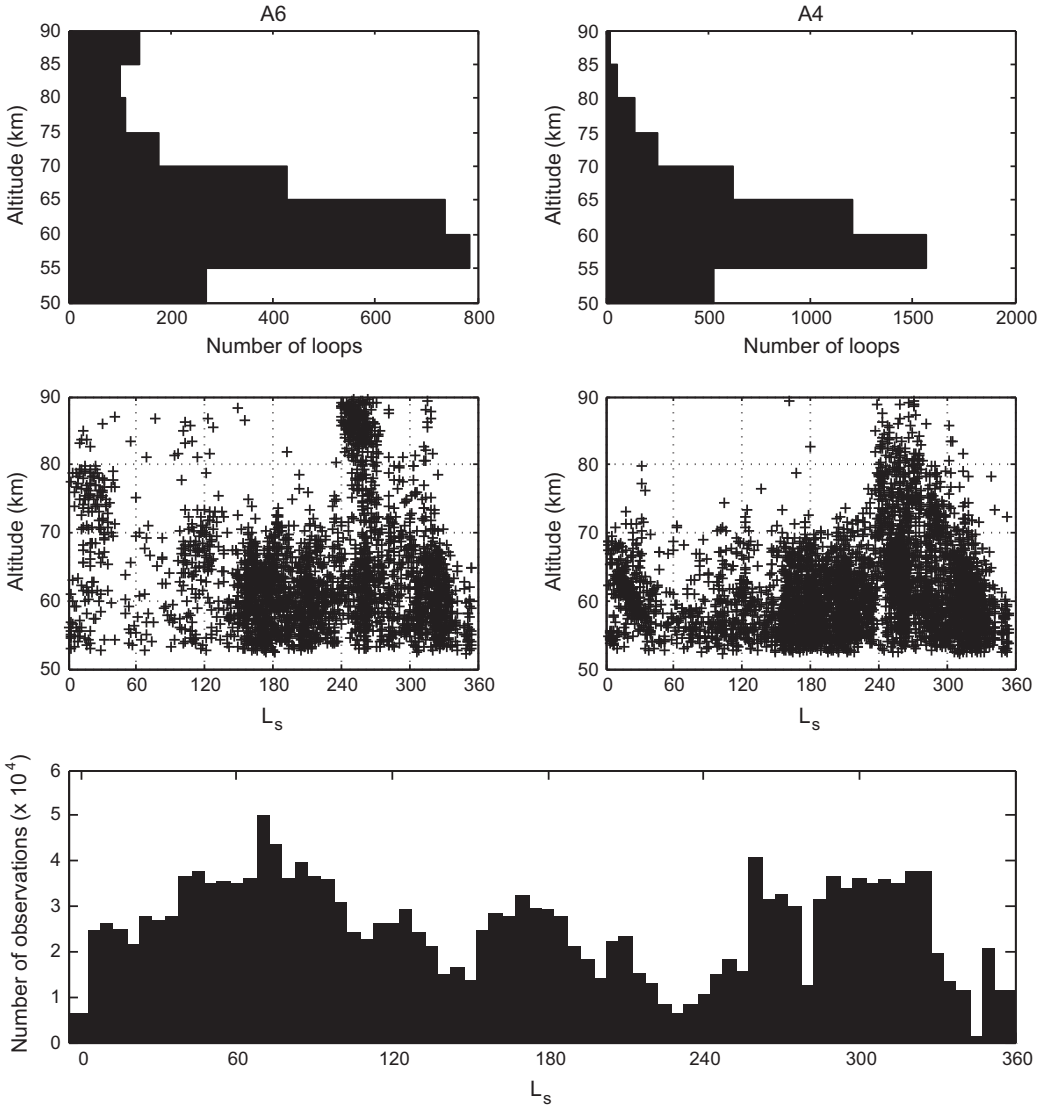

Fig. 9. Distribution of altitudes of loops detected in band A6 (upper left) and band A4 (upper right). Upper panels: number of loops detected in 5 km wide altitude bins. Mid panels: Distribution of loop altitude with solar longitude. The absence of features detected between 50 and ~53 km is an artefact of our detection method: since we consider only spectra above 50 km, features that have an upper apex close to 50 km cannot have a sufficiently long major axis to pass the aspect ratio test. Lower panel: Observation bias, i.e. Number of observations (blocks) in 5° wide bins of L_s.

Often, conditions at the exact time and altitude of a feature were not available due to the difficulty of temperature retrieval where significant aerosols are present, since these features are a strong departure from the assumed spherical symmetry that is necessary in the current retrieval scheme. Therefore, our strategy was to extract pressure and temperature retrievals that were closest in time and altitude to each feature. We discounted features that were separated from the nearest available P–T retrieval by either >300 km (~5°) ground level along-track distance or >1 km in altitude because, in those cases, conditions at the point of temperature retrieval are less likely to be representative of those in the vicinity of the feature. This separation is comparable to the vertical and horizontal scales of gravity wave perturbations, which are reported as $\lesssim$10 and 200 km, respectively (Fritts et al., 2006; Magalhães et al., 1999; Spiga et al., 2012), so it is likely that temperature within the cloud differs somewhat from our retrieval-based estimate. The application of both lateral and vertical separation filters reduced the total number of features with proximal retrievals from 2729 to 1702 (−38%) for features detected in band A6 and from 4068 to 3041 (−25%) for features in band A4.

Data points in Fig. 11 represent features for which close T(p) profiles are available and are coloured according to their deviation from the CO_2 frost point. Errors on retrieved temperatures in PDS derived data records are typically a few kelvin and rarely exceed ~6 K. Given that observed temperatures for some particularly cold features are only a few kelvin from the calculated CO_2 frost point (Fig. 11) and the likelihood of local scale variations, it is possible that their actual temperatures could lie above or below the frost point. Therefore, this comparison is necessarily somewhat qualitative as it relies on the temperature in the region of the cloud features, but not the clouds themselves. We suggest a limit of 20 K or less above the CO_2 frost point as a reasonable indicator of possible CO_2 ice formation.

In general, features detected prior to $L_s = 150°$ are colder, particularly at equatorial latitudes, where their deviation from the frost point is rarely >+20 K. However, no temperature retrievals that satisfied our separation criteria were below the CO_2 frost point. Retrievals for features detected during dust storm season generally show temperatures between 30 and 80 K higher than the CO_2 frost point, suggesting that the formation of CO_2

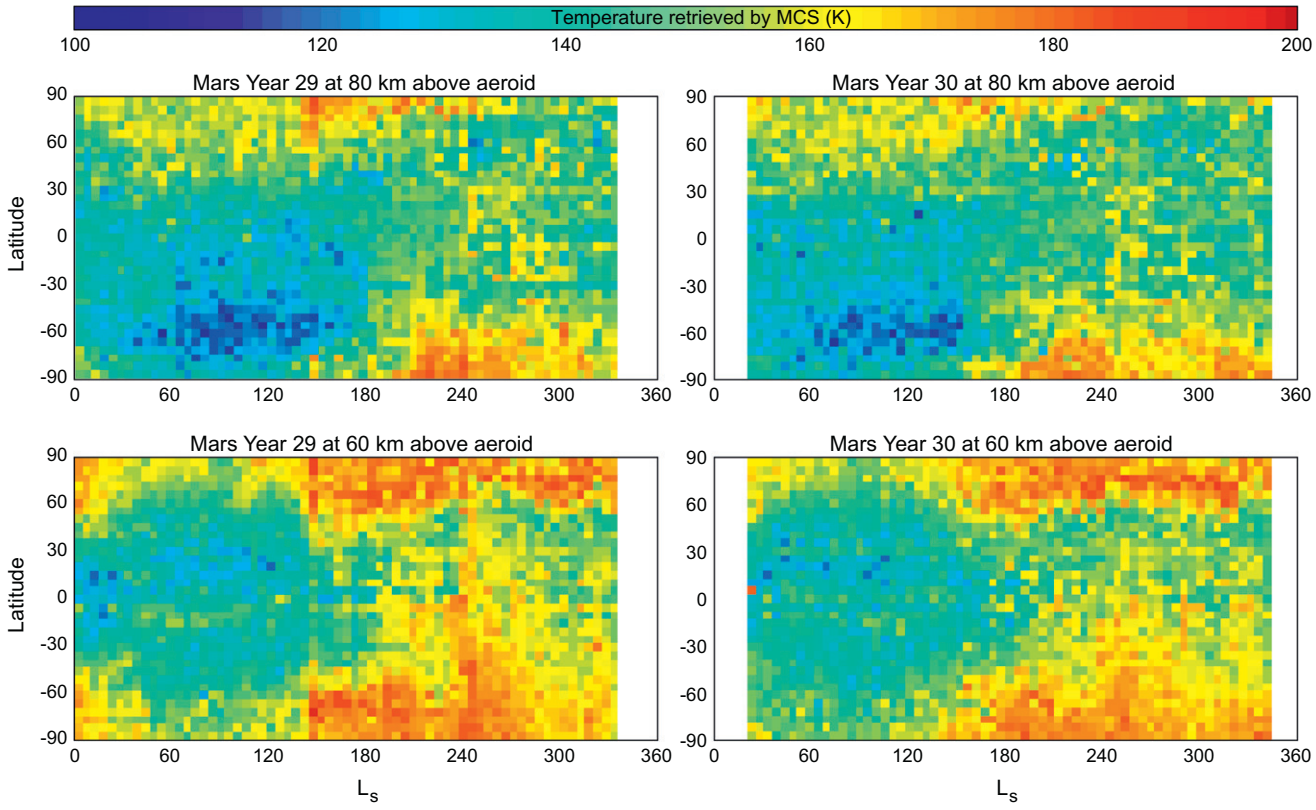

Fig. 10. Gridded average temperatures from Mars Climate Sounder derived data records over Mars years 29 and 30 at approximate altitudes of 60 and 80 km above the aeroid. Broadly, there is correlation between the seasonal–latitudinal temperature distribution observed by MCS and detected clouds (Figs. 6 and 7). Specifically, cold equatorial and southern mid-latitudes for $L_s < 150°$, and a change in regime after this point to warmer conditions during perihelion season/southern hemisphere summer. Areas of non-correlation could imply that other processes that are not sensitive to temperature play an important role in cloud formation.

ice at mesospheric altitudes is far less likely during perihelion season.

In addition to the clear seasonal dichotomy, we also observe a population of features that form at south polar latitudes between $L_s \sim 210$–$330°$ (Fig. 11). Retrieved temperatures for these features are generally >40 K above the CO_2 frost point, implying a non-CO_2 ice composition. Their location is coincident with high mesospheric temperatures in Fig. 10, which may be a result of polar warming where downwelling causes compression and adiabatic heating. Energetic convection initiated by equatorial lifting during perihelion season could be responsible for transport of dust to southern polar latitudes, which may provide nucleation sites for water ice aerosols. A similar process at the opposite season could be responsible for a smaller population of relatively warm features at north polar latitudes between $L_s \sim 90$–$150°$ (most visible in Fig. 11, panel A).

6.3. Spectral indications

The spectral channels on MCS are sufficient to provide some level of spectral discrimination between aerosols composed of CO_2 ice, H_2O ice, or dust. Accurately modelling spectra is challenging due to the large number of unconstrained parameters including particle shape, heterogeneous cloud structure, line of sight effects, scattering by low altitude clouds with heterogeneous structure and scattering from of the radiance from the unconstrained lower atmosphere.

In line with this view we adopt a conservative approach to our spectral analysis, using a single band ratio (B1/B2) to illustrate the seasonal changes in feature type. While both channels B1 and B2 are sensitive to dust and condensate extinction in the altitude range 0–80 km (McCleese et al., 2007), B2's response shape and centre make it more sensitive to ice than to dust. Therefore lower values of B1/B2 are more likely to indicate the presence of ice, rather than dust aerosols.

In order to compare broad trends in this ratio to modelled spectral characteristics, we created a large set of synthetic spectra covering plausible aerosol properties and atmospheric conditions based on the literature, which are summarised in Table 1. This combination of variables resulted in the generation of 19980 synthetic spectra for each aerosol type. The use of this comprehensive parameter space should give a realistic simulation of the spectral characteristics of the different aerosols.

Spectra were generated using the NEMESIS radiative transfer code (Irwin et al., 2008), which uses the correlated-*k* technique (Lacis and Oinas, 1991) and a spherically symmetric atmospheric geometry. The atmosphere was modelled up to ~110 km altitude and divided into 99 pressure levels, resulting in a grid spacing of ≈1 km. To increase computational efficiency, MCS filter response profiles were incorporated directly into the *k*-tables. Spectroscopic data for atmospheric gases were as described in Kleinbohl et al. (2009b). Our base atmospheric model was the COSPAR reference atmosphere, with a temperature–pressure profile from Seiff (1982) and composition from Owen (1982). In order to account for seasonally varying temperatures, the temperature at and above the aerosol layer was set to a uniform value between 90 and 200 K (in 1 K steps), which covers the full temperature range of Mars' atmosphere at these levels over a martian year. Aerosol absorption cross sections were calculated using Mie theory, with an effective variance of 20%. Refractive indices of aerosols were taken from Wolff et al. (2006) (dust), Warren (1984) (H_2O ice), and Hansen (1997) (CO_2 ice). Aerosol layers were contained within a single

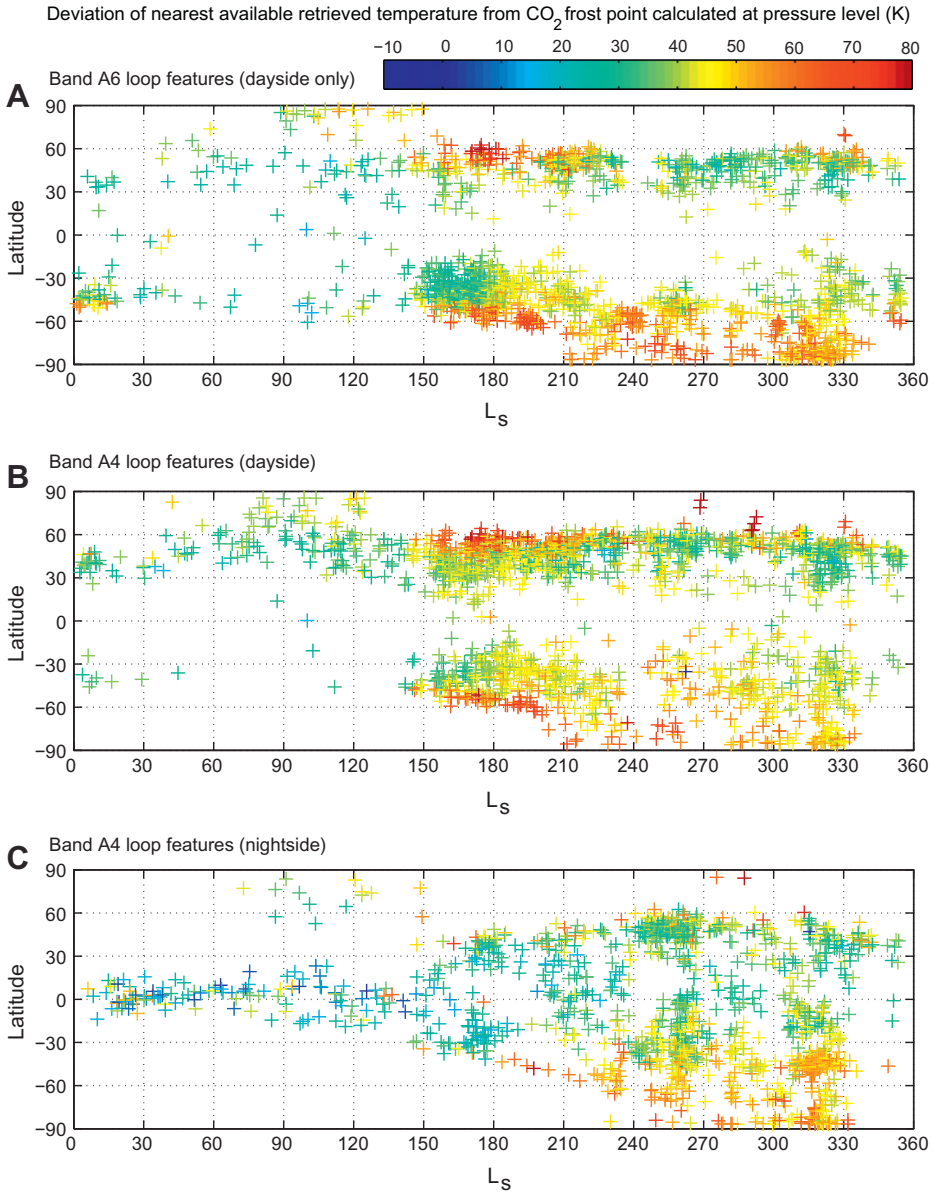

Fig. 11. Latitudes of detected loop features as a function of season in bands A4 and A6. (A) Band A6 loops. Due to the positioning of the band centre only dayside features are visible in A6. (B) Band A4 dayside loop features. (C) Band A4 nightside loop features. Data points are coloured according to the deviation of the temporally and spatially closest available temperature retrieval from the CO_2 frost point, which is calculated at the pressure level of the associated temperature retrieval. Where the nearest available retrieval was separated from the feature by more than 300 km in ground-level horizontal or 1 km vertical distance, the feature was not plotted. Mesospheric temperatures in the vicinity of cloud features at $L_s = 0$–150° are typically closer to CO_2 frost point than those in dust storm season, which are normally much higher.

pressure level (1–2 km thickness), and spectra were generated with a tangent altitude equal to the bottom of the aerosol layer. Scattering through both the cloud itself and upper atmosphere was modelled. Mixed aerosol compositions were not considered. Therefore, our channel ratios act as a guide to composition and are not by themselves definitive. This is a reasonable approach given the limited spectral information content of a channel radiometer. This simple radiative transfer analysis captures sufficient gross spectral features to make robust, yet conservative, conclusions.

We calculate the ratio B1/B2 for features classified as loops in band A6 and for synthetic spectra. We illustrate the distribution of the ratio in detected loop features compared to that for synthetic dust, H_2O and CO_2 spectra by computing histograms for each distribution (Fig. 12A). Synthetic spectra for dust almost never have B1/B2 < 0.6, while those for H_2O ice almost never show B1/B2 > 0.6. This implies that for observed features where B1/B2 < 0.6 clouds show spectral signatures most similar to synthetic spectra of CO_2 and H_2O ice. Conversely, those where B1/B2 > 0.6 appear most similar to synthetic spectra of dust and, to a lesser extent, CO_2 ice (Fig. 12A). It should be noted that the B1/B2

Table 1
Properties used to make sets of synthetic spectra for CO_2 ice, H_2O ice, and dust aerosol layers. Quantities are: z, altitude of aerosol layer; r, particle radius; τ_{843}, nadir optical depth at 843 cm^{-1} (channel A4 central wavenumber); and T_z temperature for altitudes above z. A total of 19980 spectra were made for each aerosol type.

Property	Values
z	60, 70, 80 km
r	0.1, 0.2, 0.3, 0.4, 0.5, 0.6, 0.7, 0.8, 0.9, 1.0, 1.5, 2.0 μm
τ_{843}	0.005, 0.01, 0.02, 0.04, 0.08
T_z	90–200 K (in steps of 1 K)

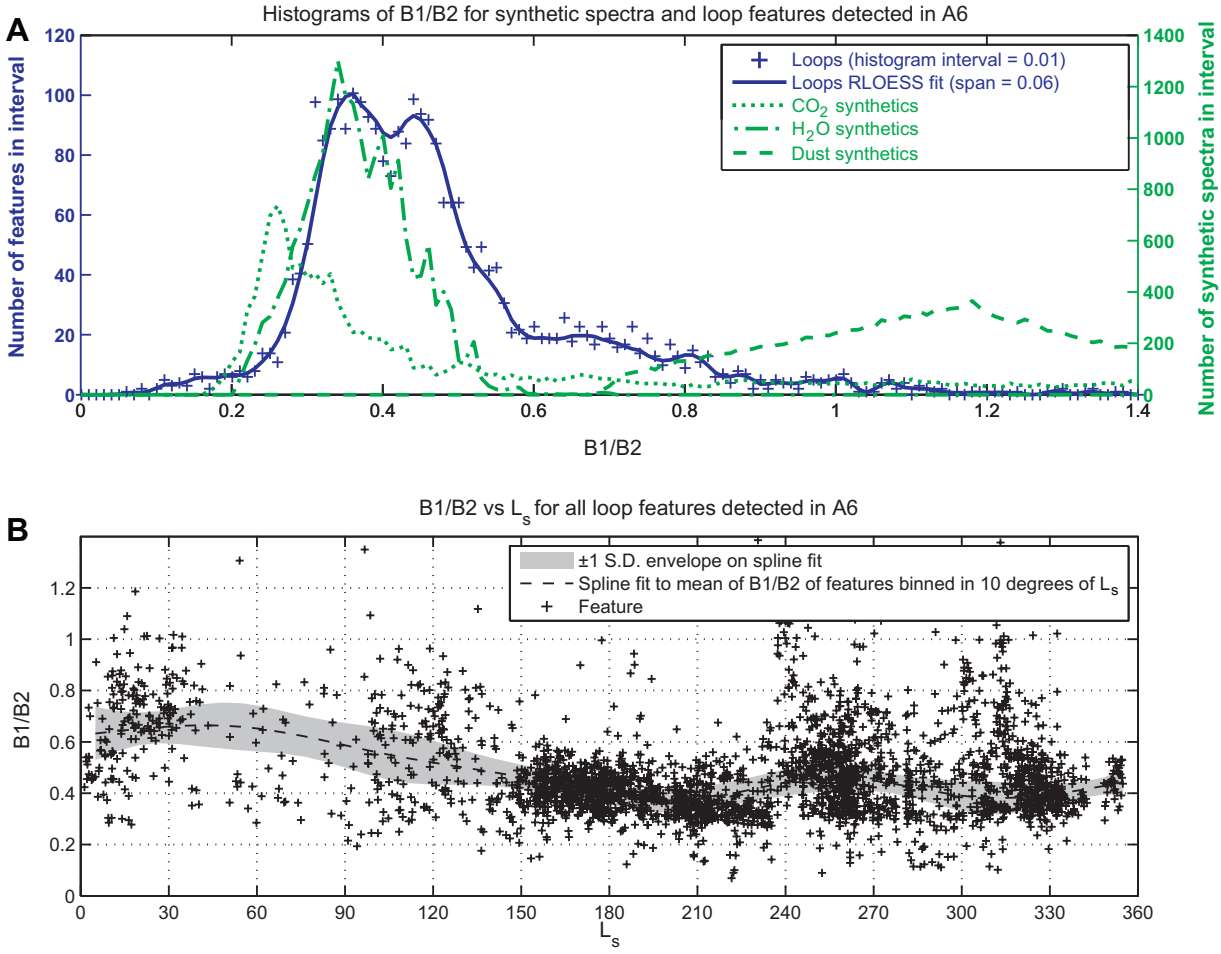

Fig. 12. (A) Histogram (and fit) of B1/B2 for features classified as loops in A6 and synthetic spectra. Histogram class width is 0.01 and the fit for observed feature histogram was performed using RLOESS, a robust local regression using weighted linear least squares and a 2nd order polynomial model. The local domain span was 0.06. No weight was given to features >6 S.D. from the mean. Eleven features with B1/B2 > 1.4 are excluded from the plot. Histogram values for synthetic spectra are represented by dotted (CO_2 ice), dashed-dotted (H_2O–ice) and dashed lines (dust). Synthetic spectra for dust almost never have B1/B2 < 0.6, while those for H_2O ice almost never show B1/B2 > 0.6. (B) B1/B2 vs L_s for features classified as loops in A6. The fit is to the mean values in 10° bins of L_s and was calculated using the tensioned spline method of Teanby (2007). Errors passed to the fitting function were 1 S.D. on the mean of each bin. Knot spacing was 50 and a small tension (γ) of 0.035 was applied to prevent unphysical overshoots characteristic of spline-based methods. Eleven features with B1/B2 values between 1.4 and ~3.5 also contributed to the fit, but the *y*-axis upper limit is fixed at 1.4 for clarity.

position of the histogram maxima of detected loop features and synthetic spectra of water ice are approximately equal and lie at B1/B2 ≈ 0.35, indicating that the largest fraction of features that we detect appear similar to water ice.

We illustrate seasonal trends in B1/B2 by fitting a tensioned spline (Teanby, 2007) to the mean values of B1/B2 in 10° bins of L_s (Fig. 12B). While the data contains considerable scatter, there is a broad seasonal trend, which indicates that B1/B2 is generally higher in features that form at L_s < 150°. The statistical dispersion indicates that dust, H_2O and CO_2 aerosols may all be present during this period because composition from a single aerosol would produce a tighter grouping of points in B1/B2. The low temperatures indicated by Fig. 11 may suggest that a significant fraction of features detected during northern summer are composed of CO_2 ice.

During northern winter/perihelion season (L_s > 150°) the majority of features detected are spectrally consistent with H_2O or CO_2 ice. High temperatures during this period indicated by Fig. 11 may reduce the likelihood of CO_2 condensation when L_s > 150°, suggesting predominantly a water ice composition for features detected during perihelion season. However, also during this season a fraction of scattered features show high B1/B2 values (>0.6, and in some cases >1), which is spectrally consistent with synthetic spectra of dust aerosols (Fig. 12A).

7. Conclusions

Using more than two Mars years of limb spectra, we detect aerosol layers in the martian mesosphere and determine their spatio-temporal distribution. We suggest composition of these layers based on nearby temperature retrievals and the diagnostic spectral ratio B1/B2. The distribution of detected features compares well to previous detections of clouds in Mars' mesosphere (Clancy et al., 2007; Määttänen et al., 2010; Montmessin et al., 2006, 2007; McConnochie et al., 2010; Scholten et al., 2010) and fills in many gaps in temporal and spatial coverage from previous instruments, which were designed predominantly for nadir observation. During N. hemisphere summer (L_s < 150°) cloud formation in the mesosphere appears relatively rare, but concentrated almost entirely at equatorial latitudes, while during dust-storm/perihelion season aerosol layers tend to form more frequently, along mid-latitude bands and preferentially in the S. hemisphere (Fig. 6).

Features detected during dust storm season at L_s > 150° generally occur in two mid-latitude belts, at altitudes <80 km (with some exceptions, see Fig. 9) and are far more numerous than those detected during aphelion season. Those detected at night (band A4, Fig. 6) appear more scattered between latitudes 60°N and 60°S than those detected during daylight hours, which tend to occur less

at the equator, though this may be due to high atmospheric opacity caused by lofted dust.

Non-dust storm equatorial features (Fig. 8B) form two longitudinal clusters between 240–300°E and 320–30°E. This is consistent with LMD-MGCM results that show daytime minimum values of T_{diff} (temperature deviation from the CO_2 frost point) between 70 and 80 km at these longitude locations, reported by González-Galindo et al. (2011) as due to the effects of topography interacting with solar forcing to create non-migrating tides. Temperature minima were also found to agree well with the location and season of clouds detected by HRSC, OMEGA, TES and THEMIS-VIS (González-Galindo et al., 2011). In addition, a cluster of mid-latitude (40–60°S) features between 40–120° longitude (Fig. 8B) is seasonally coincident with the coldest temperatures observed by MCS at 80 km (Fig. 10, upper panels).

Cloud production during both seasons appears higher during several well-defined time periods during the martian year. Higher formation frequencies of equatorial aerosol layers occur during northern hemisphere spring (L_s = 0–60°), particularly in detections using band A6 dayside and band A4 nightside data.

We have compared the statistical distribution of a simple spectral parameterization (B1/B2) in observed feature spectra with that of synthetic spectra of dust, H_2O ice and CO_2 ice aerosols (Fig. 12). We find that values of B1/B2 > 0.6 likely indicate the presence of dust or CO_2 ice, while those < 0.6 are typical for water or CO_2 ice. We find a large number of features appear similar to synthetic spectra of water–ice, particularly during perihelion/dust storm season (Fig. 12), consistent with temperatures 30–80 K above the CO_2 frost point observed for those features (Fig. 11). However, a significant number of features during this time show values of B1/B2 > 1, indicating a spectral similarity to dust. During northern summer (L_s < 150°) clouds are predominantly equatorial and appear spectrally similar to H_2O or CO_2 ice, but a significant fraction have proximal temperature retrievals that are within a few degrees of the CO_2 frost point, indicating a CO_2 composition is possible for these features.

Longitudinal and temporal clustering could be related to the broad effects of global circulation, which may act as transport mechanisms for dust nuclei. However, for sub-CO_2 frost point conditions to form a mechanism for further cooling is probably required. As has been suggested (González-Galindo et al., 2011; Määttänen et al., 2010; Spiga et al., 2012), this could be the interaction between cold conditions imposed by global circulation and the propagation to the mesosphere of small-scale dynamics such as gravity waves and thermal tides to further reduce temperatures adiabatically in local rarefactions.

While our detection technique has enabled spatiotemporal mapping and preliminary spectral identification of high radiance mesospheric aerosol layers there remains scope for improvement to our detection method and spectral analysis. Specifically, we envisage that any future work should take advantage of all of MCS's available channels and account for the effects of scattering from the lower atmosphere in order to better constrain the composition and microphysical properties of aerosol particles. However, at the present time more in depth interpretation is limited by the lack of temperature profiles with the clouds themselves.

Acknowledgments

This work was funded by the UK Science and Technologies Facilities Council (STFC) and the Leverhulme Trust. Thanks are due to David Kass for insightful feedback on an early draft of the manuscript, and to two anonymous reviewers whose comments helped to improve the paper.

References

Anderson, E.M., Leovy, C.B., 1978. Mariner 9 television limb observations of dust and ice hazes on Mars. J. Atmos. Sci. 35, 1861–1883.
Cantor, B.A., 2007. Moc observations of the 2001 Mars planet-encircling dust storm. Icarus 186, 60–96.
Clancy, R.T., Sandor, B.J., 1998. CO_2 ice clouds in the upper atmosphere of Mars. Geophys. Res. Lett. 25 (4), 489–492.
Clancy, R.T., Wolff, M.J., Whitney, B.A., Cantor, B.A., 2003. Vertical distribution of dust optical depth during the 2001 planet encircling storm from a spherical radiative transfer analysis of MOC LIMB images. In: Sixth Int. Conf. Mars, Lunar and Planet. Inst., Pasadena, Calif. Abstract 3205.
Clancy, R.T., Wolff, M., Whitney, B.A., Cantor, B.A., 2004. The distribution of high altitude (70 km) ice clouds in the Mars atmosphere from MGS TES and MOC LIMB observations. Bull. Am. Astron. Soc. 36. Abstract 1128.
Clancy, R.T., Wolff, M.J., Whitney, B.A., Cantor, B.A., Smith, M.D., 2007. Mars equatorial mesospheric clouds: Global occurrence and physical properties from Mars Global Surveyor thermal emission spectrometer and Mars Orbiter camera limb observations. J. Geophys. Res. 112 (E04004), 1–18.
Colaprete, A., Barnes, J.R., Haberle, R.M., Montmessin, F., 2008. CO_2 clouds, cape and convection on Mars: Observations and general circulation modeling. Planet. Space Sci. 56, 150–180.
Deming, D., Espenak, F., Jennings, D., Kostiuk, T., Mumma, M., Zipoy, D., 1983. Observations of the 10 μm natural laser emission from the mesospheres of Mars and Venus. Icarus 55, 347–355.
Fedorova, A.A., Korablev, O.I., Bertaux, J.-L., Rodin, A.V., Montmessin, F., Belyaev, D.A., Reberac, A., 2009. Solar infrared occultation observations by SPICAM experiment on Mars-express: Simultaneous measurements of the vertical distributions of H_2O, CO_2 and aerosol. Icarus 200, 96–117.
Forbes, J.M., Miyahara, S., 2006. Solar semidiurnal tide in the dusty atmosphere of Mars. J. Atmos. Sci. 63, 1798–1817.
Forget, F., Hourdin, F., Fournier, R., Hourdin, C., Talagrand, O., 1999. Improved general circulation models of the martian atmosphere from the surface to above 80 km. J. Geophys. Res. Planet. 104, 24155–24176.
Forget, F. et al., 2008. Modeling the martian atmosphere with the LMD global climate model. In: The Third International Workshop on the Mars Atmosphere: Modeling and Observations (Williamsburg, VA) (9054).
Formisano, V., Maturilli, A., Giuranna, M., D'Aversa, E., Lopez-Valverde, M.A., 2006. Observations of non-LTE emission at 4–5 μm with the planetary Fourier spectrometer aboard the Mars Express mission. Icarus 182, 51–67.
Fritts, D.C., Wang, L., Tolson, R.H., 2006. Mean and gravity wave structures and variability in the Mars upper atmosphere inferred from Mars Global Surveyor and Mars Odyssey aerobraking densities. J. Geophys. Res. 111 (A12304), 1–14.
Gondet, B., Bibring, J.P., Vincendon, M., 2012. Monitoring the mesospheric CO_2 ice clouds by OMEGA/MEx. In EGU General Assembly 2012, Vienna, Austria, p. 9800.
González-Galindo, F., Määttänen, A., Forget, F., Spiga, A., 2011. The martian mesosphere as revealed by CO_2 cloud observations and general circulation modeling. Icarus 216, 10–22.
Hansen, G.B., 1997. The infrared absorption spectrum of carbon dioxide ice from 1.8 to 333 μm. J. Geophys. Res. 102, 21569–21588.
Heavens, N.G., Richardson, M.I., Lawson, W.G., Lee, C., McCleese, D.J., Kass, D.M., Kleinböhl, A., Schofield, J.T., Abdou, W.A., Shirley, J.H., 2010. Convective instability in the martian middle atmosphere. Icarus 208, 574–589.
Henderson, V., Sayfi, E., McCleese, D.J., Beebe, R., Grayzeck, E., 2007. Mars Climate Sounder experiment data record software interface specification (v1.2). Jet Propulsion Laboratory (JPL D-3729).
Herr, K.C., Pimentel, G.C., 1970. Evidence for solid carbon dioxide in the upper atmosphere of Mars. Science 167, 47–49.
Holton, J.R., 2004. An Introduction to Dynamic Meteorology. Elsevier, Amsterdam, pp. 295–296.
Inada, A., Richardson, M.I., McConnochie, T.H., Strausberg, M.J., Wang, H., Bell (III), J.F., 2007. High-resolution atmospheric observations by the Mars Odyssey thermal emission imaging system. Icarus 192, 378–395.
Irwin, P. et al., 2008. The NEMESIS planetary atmosphere radiative transfer and retrieval tool. J. Quan. Spec. Rad. Transfer 109, 1136–1150.
Jaquin, F., 1988. Very high elevation water ice clouds on Mars: Their morphology and temporal behaviour. In: MECA Workshop on Atmospheric H_2O Observations of Earth and Mars: Physical Processes, Measurements, and Interpretations LPI N89-25790 (19–91), pp. 61–64.
Jaquin, F., Gierasch, P., Kahn, R., 1986. The vertical structure of limb hazes in the martian atmosphere. Icarus 68, 442–461.
Johnson, M.A., Betz, A.L., McLaren, R.A., Townes, C.H., Sutton, E.C., 1976. Nonthermal 10 μm CO_2 emission lines in the atmospheres of Mars and Venus. Astrophys. J. 208, L145–L148.
Kass, D.M., Abdou, W.A., McCleese, D.J., Schofield, J.T., Määttänen, A., 2011. MCS climatology of detached, localized haze layers. In: Forget, F., Millour, E. (Eds.), Fourth International Workshop on the Mars Atmosphere: Modelling and Observations. pp. 400–403.
Kleinbohl, A. et al., 2009a. Mars Climate Sounder limb profile retrieval of atmospheric temperature, pressure, and dust and water ice opacity. J. Geophys. Res. 114 (E10006), 1–30.
Kleinbohl, A. et al., 2009b. Mars Climate Sounder limb profile retrieval of atmospheric temperature, pressure, and dust and water ice opacity. J. Geophys. Res., E114.

Lacis, A.A., Oinas, V., 1991. A description of the correlated k distribution method for modeling nongray gaseous absorption, thermal emission, and multiple-scattering in vertically inhomogeneous atmospheres. J. Geophys. Res. 96 (D5), 9027–9063.

Lee, C. et al., 2009. Thermal tides in the martian middle atmosphere as seen by the Mars Climate Sounder. J. Geophys. Res. 114 (E03005), 1–16.

Lide, D.R. (Ed.), 1995. CRC Handbook of Chemistry and Physics, 76th ed. CRC Press, Inc., Boca Raton.

Määttänen, A., Montmessin, F., Gondet, B., Scholten, F., Hoffmann, H., González-Galindo, F., Spiga, A., Forget, F., Hauber, E., Neukum, G., Bibring, J.-P., Bertaux, J.-L., 2010. Mapping the mesospheric CO_2 clouds on Mars: MEx/OMEGA and MEx/HRSC observations and challenges for atmospheric models. Icarus 209, 452–469.

Magalhães, J.A., Schofield, J.T., Seiff, A., 1999. Results of the Mars pathfinder atmospheric structure investigation. J. Geophys. Res. 104 (E4), 8943–8955.

McCleese, D.J. et al., 2007. Mars Climate Sounder: An investigation of thermal and water vapour structure, dust and condensate distributions in the atmosphere, and energy balance of the polar regions. J. Geophys. Res. 112 (E05S06), 1–16.

McConnochie, T.H., Bell (III), J.F., Savransky, D., Wolff, M.J., Christensen, P.R., Richardson, M.I., Titus, T.N., 2005. THEMIS-VIS measurements of the altitude and velocity of clouds in the martian mesosphere. In: AGU Fall Meeting, USA. pp. P21–E03.

McConnochie, T.H., Bell (III), J.F., Savransky, D., Wolff, M.J., Toigo, A.D., Wang, H., Richardson, M.I., Christensen, P.R., 2010. THEMIS-VIS observations of clouds in the martian mesosphere: Altitudes, wind speeds and decameter-scale morphology. Icarus 210, 545–565.

Montmessin, F., Bertaux, J.-L., Quémerais, E., Korablev, O., Rannou, P., Forget, F., Perrier, S., Fussen, D., Lebonnois, S., Rébérac, A., Dimarellis, E., 2006. Subvisible CO_2 ice clouds detected in the mesosphere of Mars. Icarus 183, 403–410.

Montmessin, F., Gondet, B., Bibring, J.-P., Langevin, Y., Drossart, P., Forget, F., 2007. Hyperspectral imaging of convective CO_2 ice clouds in the equatorial mesosphere of Mars. J. Geophys. Res. 112 (E11S90), 1–14.

Owen, T., 1982. The composition of the martian atmosphere. Adv. Space Res. 2, 75–80.

Schofield, J.T. et al., 1997. The Mars pathfinder atmospheric structure investigation/meteorology (ASI/MET) experiment. Science 278, 1752–1757.

Scholten, F., Hoffmann, H., Määttänen, A., Montmessin, F., Gondet, B., Hauber, E., 2010. Concatenation of HRSC colour and OMEGA data for the determination and 3d-parameterization of high-altitude CO_2 clouds in the martian atmosphere. Planet. Space Sci. 58, 1207–1214.

Seiff, A., 1982. Post-Viking models for the structure of the summer atmosphere of Mars. Adv. Space Res. 2, 3–17.

Seiff, A., Kirk, D.B., 1977. Structure of the atmosphere of Mars in summer at mid-latitudes. J. Geophys. Res. 82, 4352–4378.

Smith, P.H. et al., 1997. Results from the Mars Pathfinder camera. Science 278, 1758–1764.

Smith, M.D., 2003. TES limb-geometry observations of aerosols. In: Sixth Int. Conf. Mars, Lunar and Planet. Inst., Pasadena, Calif. (3174).

Smith, M.D., 2004. Interannual variability in TES atmospheric observations of Mars during 1999–2003. Icarus 167 (1), 148–165.

Spiga, A., Forget, F., 2009. A new model to simulate the martian mesoscale and microscale atmospheric circulation: Validation and first results. J. Geophys. Res. 114 (E02009), 1–26.

Spiga, A., González-Galindo, F., López-Valverde, M.-Á., Forget, F., 2012. Gravity waves, cold pockets and CO_2 clouds in the martian mesosphere. Geophys. Res. Lett. 39 (L02201), 1–5.

Teanby, N.A., 2007. Constrained smoothing of noisy data using splines in tension. Math. Geol. 39, 419–434.

Teanby, N.A., 2009. Intersection between spacecraft viewing vectors and digital elevation models. Comput. Geosci. 35, 566–578.

Vincendon, M., Pilorget, C., Gondet, B., Murchie, S., Bibring, J.-P., 2011. New near-ir observations of mesospheric CO_2 and H_2O clouds on Mars. J. Geophys. Res. 116 (E00J02), 1–30.

Warren, S.G., 1984. Optical constants of ice from the ultraviolet to the microwave. Appl. Opt. 23, 1206–1225.

Wolff, M.J. et al., 2006. Constraints on dust aerosols from the Mars Exploration Rovers using MGS overflights and Mini-TES. J. Geophys. Res. 111, E12S17.

Zuber, M.T. et al., 1992. The Mars observer laser altimeter investigation. J. Geophys. Res. 97 (E5), 7781–7797.